

Computational tool

Quantifying Cytoplasmic Streaming in *C. elegans* Embryos by DIC Object Tracking (DICOT)

Anushree R. Chaphalkar¹, Yash K. Jawale¹, Dhruv Khatri¹, and Chaitanya A. Athale^{1,*}

¹Div. of Biology, IISER Pune, Dr. Homi Bhabha Road, Pashan, Pune 411008, India.

*Correspondence: cathale@iiserpune.ac.in

ABSTRACT In contrast with fluorescence microscopy, label-free imaging techniques such as Differential Interference Contrast (DIC) allow the observation of cells and large sub-cellular structures in their native, unperturbed states with minimal exposure to light. Combined with robust image-analysis routines that can automatically quantify features from DIC images, this has been used to gain insights into cellular and sub-cellular processes. While many methods convert DIC into phase-like images, we have previously demonstrated quantification of bacterial cell sizes using morphological properties of the DIC images. Here, we describe an improved segmentation method that successfully detects DIC objects both *in vitro* and *in vivo* and combined with a minimal-distance 2D tracking method, allows us to infer sub-cellular dynamics. We test this method on the a time-series of first asymmetric cell division in *Caenorhabditis elegans* focussed on the mid-plane of the embryo. By tracking the birefringent yolk granules in the cytoplasm, we produce a 2D map of oscillatory dynamics of the spindle. We also extract the viscosity of a fluid from a DIC time-series of spherical beads diffusing in glycerol solutions of increasing concentration, demonstrating the utility of our method for microrheology in environments that mimic the cell. Together we demonstrate a novel approach to DIC image time-series object detection and tracking that could have implications for a better understanding of sub-cellular mechanics, using label-free methods.

SIGNIFICANCE

INTRODUCTION

Label-free microscopy is widely used to study transparent cells and tissues. In particular, differential interference contrast (DIC) or Nomarski (1) and phase-contrast microscopy (2) are standard modes built into biological microscopes to generate image contrast using inherent features such as the anisotropy of refractive index and density. While fluorescence microscopy offers the advantage of molecular specificity, the phototoxicity resulting from such an approach in live-imaging can alter cell physiology (3). Due to the inherent advantages of reduced light exposure and minimal intervention in the sample, label-free *in vivo* microscopy combined with computational image analysis continues to be relevant. Image segmentation of label-free images is relatively simpler with phase contrast, since it involves distinguishing dark objects against a bright background. As a result, a wide variety of computational methods have been developed to quantify phase contrast images of cellular and sub-cellular objects (4–7). Objects in DIC images on the other hand, are represented as a combination of light and dark regions giving a pseudo-3D effect. Segmentation of such images is more involved, with previous approaches relying on either converting them to ‘pseudo-phase’ (8), or extracting low-level information such as gradient (9, 10), shear direction (11, 12) and brightness fluctuations (13). While shape-specific methods have been successfully used for tracking the dynamics of filopodia (14) and microtubules (MTs) (13, 15), they are limited in their utility. The absence of a robust and general solution to detect intracellular structures in DIC at high particle densities has hindered further quantification of label free images.

Caenorhabditis elegans embryos are ideal samples for *in vivo* computational imaging in DIC since they are optically transparent and lack pigments. DIC microscopy based mutational screens have been used to understand embryonic cell divisions (16) and spindle mechanics (17). Algorithms used to identify features in *C. elegans* embryos include a shortest path method to automatically identify embryo stages and quantify boundary dynamics during divisions (18, 19). Similarly, active contours have been used to track spindle dynamics (20, 21). The analysis of intracellular dynamics by segmentation-based approaches has been restricted to quantifying centrosome positional dynamics (17, 22, 23). At the same time, detailed theoretical models of the mechanics anaphase spindles and their oscillations in *C. elegans* based on molecular motors and MTs have been developed (24–26). However, a comparison between theoretical predictions and experiments continues to be limited by the methods

available for non-invasive measurement of intracellular mechanics. While label-free quantitative microscopy could address this need, it requires the development of methods for precise segmentation in a crowded environment from such images.

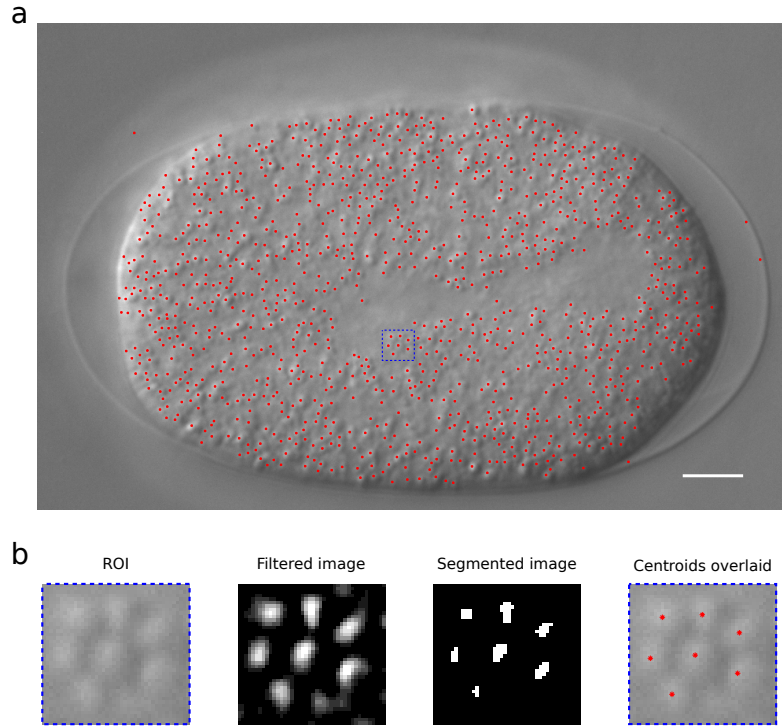


Figure 1: Detecting yolk-granules in *C. elegans* embryo in DIC. **(a)** The yolk granules of a *C. elegans* embryo at the one-cell stage in DIC microscopy from the mid-plane are segmented using a novel Scaling of Gaussian (SoG) method. Asterisks (*) mark the detected granules. Scale: 5 μm . **(b)** An ROI of the embryo image (box with dashed blue line from **(a)**) demonstrates the workflow: 2D filtering (filter parameters: $k_{size} = 9$ and $\sigma = 1.25$), segmentation using the modified Otsu's method and resulting in centroids of the detected granules (red asterisks) overlaid on the original image.

Here, we describe a DIC object tracking (DICOT) method that combines a novel filtering approach that we refer to as Scaling of Gaussian (SoG). Combined with a distance-based single particle tracking approach, we employ it to analyze *in vivo* cytoplasmic streaming dynamics in a one-celled *C. elegans* embryo and as a means of estimating viscosity from bead diffusion in glycerol solutions.

MATERIALS AND METHODS

DIC segmentation and tracking

A mean subtracted 2D Gaussian filter (h'_G) is calculated as described in the expression:

$$h'_G = h_G(n_1, n_2) - \langle h_G \rangle \quad (1)$$

where the filter mean $\langle h_G \rangle = [\sum_{n_1} \sum_{n_2} h_G(n_1, n_2)]/[n_1 n_2]$ and h_G is the function:

$$h_G(n_1, n_2) = \frac{h''_G(n_1, n_2)}{\sum_{n_1} \sum_{n_2} h''_G} \quad (2)$$

with the term h''_G representing the Gaussian:

$$h''_G(n_1, n_2) = e^{-\frac{(n_1^2 + n_2^2)}{2\sigma^2}} \quad (3)$$

Here n_i indicates dimension with $i \in (1, 2)$ and σ is the standard deviation of the distribution. The dimensions in rows and columns are uniform and determined by the kernel size (k_{size}) as follows:

$$n_i = \frac{k_{size} - 1}{2}, \quad i \in (1, 2) \quad (4)$$

The values of k_{size} and σ are optimized based on object size. In case of yolk granules in *C. elegans* embryos, k_{size} was 9 and σ was 1.25 and resulted in distinct peaks at the center of the granules (Fig. 3(b)).

We finally obtain the scaled filter h_{SoG} by taking the difference of the filter h'_G (Equation 1) scaled by the mean value and modified further with the product of a sensitivity factor ϕ and the mean as follows:

$$h_{SoG}(n_1, n_2) = \begin{cases} h'_G(n_1, n_2) - \phi \cdot \langle h_G \rangle, & \text{for bright objects} \\ -h'_G(n_1, n_2) - \phi \cdot \langle h_G \rangle, & \text{for dark objects} \end{cases} \quad (5)$$

DIC images are then filtered using this Scaling of Gaussian filter, SoG (Equation 5), to generated a filtered image invoking this function with `imfilter` in MATLAB (Mathworks Inc., MA, USA). The steps involved in the process are described in the algorithm box 1.

Algorithm 1 Filter the image by SoG and segment it

```

Image, Img ← INPUT(filename)
Kernel-size, ksize ← INPUT(int)
3: Kernel-spread, σ ← INPUT(float)
   ObjectType, λ ← INPUT(bright=1,dark=-1)
   Sensitivity, φ ← INPUT(float)
6: Strength of threshold, p ← INPUT(int)
   h''G(n1, n2) = exp-(n12+n22)/2σ2
   hG(n1, n2) =  $\frac{h''_G(n_1, n_2)}{\sum_{n_1} \sum_{n_2} h''_G}$ 
9: ⟨hG⟩ = [Σn1 Σn2 hG] / n1 n2
   h(n1, n2) = hG(n1, n2) - ⟨hG⟩
   hSoG = λh - φ⟨hG⟩
12: imFiltered ← hSoG(n1, n2) ⊗ Img(j - n1 + 1, k - n2 + 1)
    Threshold, τ ← Otsu(imFiltered)

15: if imFiltered(j,k)>  $\sqrt[p]{\tau}$  then
      imFiltered(j,k)← 1
    else
18:   imFiltered(j,k) ← 0
  end if
  
```

The filtered contrast-adjusted image is segmented by using the p^{th} root of the value output by Otsu's method, τ . We find $\sqrt[\mathfrak{p}]{\tau}$, i.e. $p = 2$, to be optimal for the stringent detection of objects.

Segmentation results in multiple centroids at each time point, that are connected to form tracks based on two input parameters: (i) search radius (r_s) to define the local neighborhood that depends on particle velocity and (ii) a minimal time frames (T_{min}) which a track spans. The pair-wise distance $d_j(\Delta t)$ between every j^{th} centroid in successive frames t and $t + \Delta t$ are linked if the minimal distance is less than the search radius r_s . Centroids that do not form a part of any trajectory are treated as new start-points. To avoid artefacts due to poor statistics, short tracks are eliminated if they span less than T_{min} number of frames.

Embryo time-series

Multiple time-series of *C. elegans* N2 embryos were taken from a published database (http://www.ens-lyon.fr/LBMC/NematodeCell/2010/12/n2_15/) reported by Valfort et al. (27). Typically 400-500 frames were analyzed, by selecting a subset of frames corresponding to the onset of anaphase spindle oscillations. The time interval between frames is 0.5 s.

Microscopy of bead suspensions in glycerol

Glycerol (99% GC, Sigma-Aldrich Inc., USA) solutions in water with increasing concentrations 0, 10, 20, 30 and 40% (vol/vol) were used to resuspend monodisperse polystyrene beads (NIST Traceable Particle Size Standards, Bangs Laboratories Inc, IN, USA) of a diameter of 1 μm . For diffusion measurements the beads were diluted 1:100 (vol/vol) to get sufficient separation, so their mobility can be considered to be independent of crowding effects. The solution containing the bead suspension was flowed into a double-backed tape chamber (dimensions - 1 cm x 1 cm x 0.01 cm) sandwiched between a slide and a coverslip (Medicos Supplies, Pune India). Samples were imaged using a 40x (N.A. 0.9) lens on a Nikon Eclipse Ti-E inverted microscope (Nikon Corp., Japan) at 27°C by a temperature control system (Oko Lab, Italy). Images were acquired every 0.5 s for 1 minute with an Andor Clara2 CCD camera (Andor Technology, Belfast, NI, U.K.).

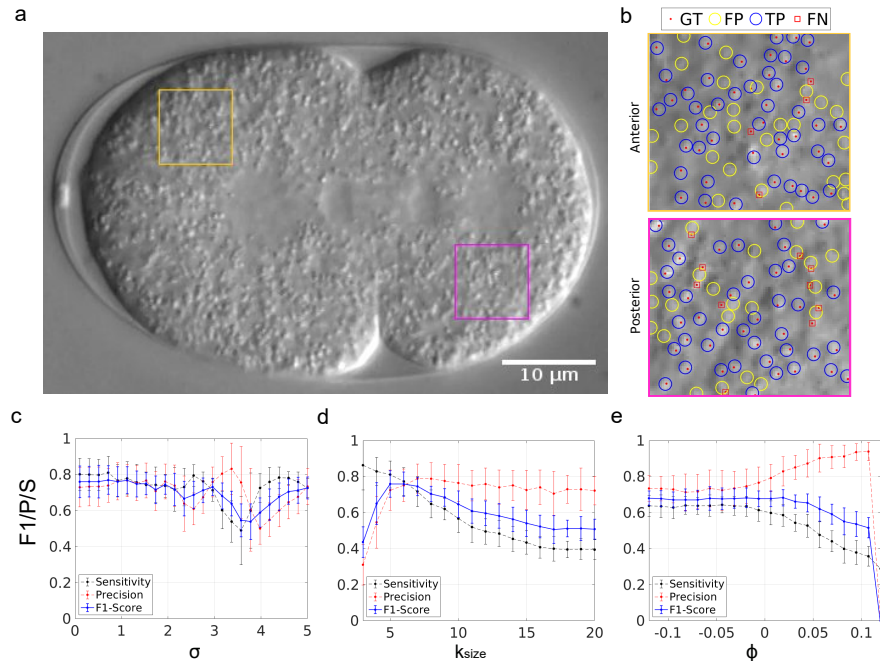


Figure 2: Precision of yolk granule detection in DIC. (a) Regions of interest (ROIs) from the anterior (ochre) and posterior (cyan) regions of a DIC image time series of a *C. elegans* were used to estimate (b) the ground truth through manual annotation of granules (red dots) and classify algorithm-based detections as either *true positives*: detected by the algorithm as well as manually (blue circles), *false positives*: those identified by the algorithm but not by eye (yellow circles) and *false negatives*: those that were identified manually but the algorithm failed to detect (red boxes). (c-e) The precision, P (black dashes), sensitivity, S (red dashes) and the F1-score (blue lines) of detection are plotted to examine the effect of three different parameters input to DICOT namely (c) the standard deviation of the filter σ , (d) the filter size k_{size} and (e) the sensitivity factor ϕ .

Data analysis

The tracks of yolk granules, x and y-positions with time, were used to calculate the distance from their respective origins in x (Δx) and y (Δy). Based on the apparent axis along which granules in a region were maximally displaced, A(nterior), P(osterior), or one of the T(ransverse) axes- T1 or T2- their Δx and Δy values plotted over time were averaged for the region. The frequency of oscillation was estimated using a fast Fourier transform (FFT). An average curve estimated for each region as follows:

(a) Shift the origin of the position time series of the yolk granules, $r_{j,t}$ (where r is either the x- or y-position) with respect to their initial positions in x (Δx) and y (Δy) resulting in a new series $r_{j,t}^*$:

$$i = 0 \begin{cases} r_{j,t}^* = & r_{j,t} - r_{j,1} \\ \tilde{r}_{(i=0)} = & \sum_t \frac{\sum_{j|t} r_{j,t}^*}{n_{j|t}} \end{cases} \quad (6)$$

where n is the number of tracks at a given time point t and j represents the identity of the track.

(b) Calculate the average time series \bar{r}_i for the i^{th} iteration by estimating the deviation of every particle from average curve obtained at the previous iteration ($i - 1$), subtracting the mean deviation ($\langle \Delta r_{j,t} \rangle$) and averaging over each track at a given time point ($n_{j|t}$) for all time points as follows:

$$\begin{cases} \Delta r_{j,t} = r_{j,t} - \bar{r}_{i-1} \\ r_{j,t}^* = r_{j,t} - \langle \Delta r_{j,t} \rangle \\ \bar{r}_i = \sum_t^T \frac{\sum_{j|t} r_{j,t}^*}{n_{j|t}} \end{cases} \quad (7)$$

(c) Consider the curve to be the optimal average curve and stop the iteration, when the global deviation across all tracks N is smaller than a threshold value δ :

$$i++, \text{ iff } \left\{ \frac{\sum_j^N \langle \Delta r_{j,t} \rangle}{N} \geq \delta \right\} \quad (8)$$

We find the global deviation saturates for $\delta < 10^{-4}$ within 5 to 10 iterations (Fig. S3). All data analysis was performed using code written in MATLAB R2017b (Mathworks Inc., MA, USA).

Estimating the diffusion coefficient of bead mobility

The effective diffusion coefficient of bead motility was estimated from a fit to the mean squared displacement (MSD) plot as a function of time interval, as described previously (28, 29). The diffusion coefficient D was estimated by fitting the anomalous diffusion model $MSD = 4 \cdot D_{eff} \cdot t^\alpha$ to the MSD data using a Levenberg-Marquardt non-linear least square routine implemented in SciPy Anaconda Distribution under Python 3.6. Only those bead trajectories were analyzed, whose path length were greater than $\sim 7 \mu\text{m}$ to avoid sampling static particles. The anomaly parameter α was found to be ~ 1 , indicating diffusion without drift or restriction.

As an alternative method to measure the diffusion coefficient of beads is based on a method originally described by Perrin (30). The displacement along the x- (Δx) and y-axes (Δy) for every successive step of each trajectory were plotted in a frequency histogram and fit to a standard Gaussian expression:

$$P(\Delta x) = \frac{1}{\sigma \sqrt{2\pi t}} \exp^{-\Delta x^2 / 2\sigma^2} \quad (9)$$

where σ is the standard deviation that for 1D diffusion is related to the diffusion coefficient by $\sigma = \sqrt{2Dt}$.

The viscosity was estimated from Stokes-Einstein relation $D = k_B T / 6\pi\eta r$ where the radius of the beads (r) was $0.5 \mu\text{m}$.

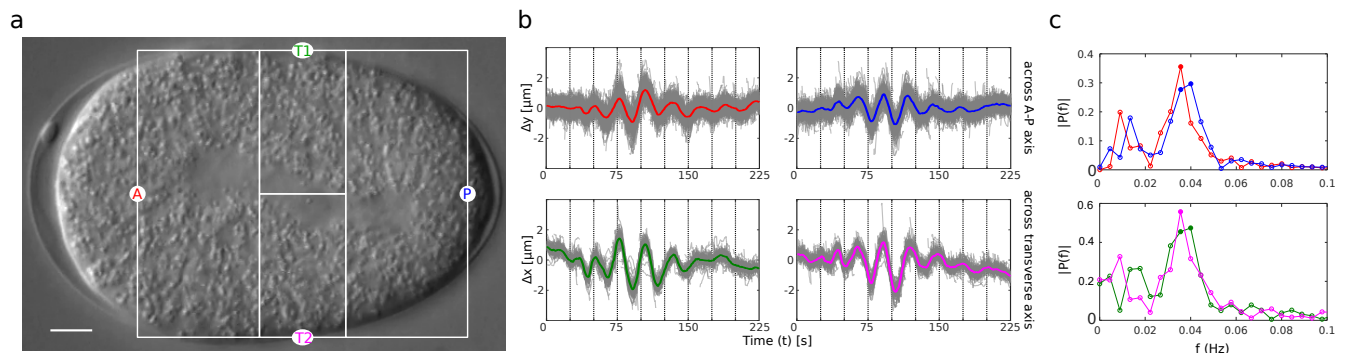


Figure 3: *In vivo* microrheology of *C. elegans* yolk granule mobility. (a) A DIC image of the mid-plane of a *C. elegans* embryo prior to division is marked to highlight four spatial regions of the embryo, the anterior- A (red), posterior- P (blue) and two transverse regions T1(green) and T2 (magenta) that were analyzed. The image-time series is taken from a previous report by Valfort et al. (27). Scale bar: 5 μm . (b) The change in position along x (Δx) and y (Δy) axes of individual granule trajectories are plotted a function of time (grey lines) for movement across the AP and transverse axes. Colored lines represent mean trajectories for the A (red), P (blue), T1(green) and T2 (magenta) regions. (c) The probability distribution of oscillatory frequencies from FFT analysis of mean trajectories are plotted for A (red), P (blue), T1 (green) and T2 (magenta) regions.

Code performance and availability.

A typical time-series with 300 frames of 488x290 pixels required 5 to 10 minutes to process with 200 particles per frame on a Linux Workstation with two Intel Xeon processors (2.20 GHz) and 64 GB RAM. The program has been uploaded as OpenSource on GitHub and can be accessed at:

RESULTS AND DISCUSSION

Testing the detection accuracy of intracellular granules in DIC images

The quality of single particle tracking (SPT) often depends on the accuracy of the object detection. In order to achieve high-accuracy tracking, we combine a novel filtering approach - scaling of Gaussian (SoG) - with standard thresholding based on Otsu's method to detect objects in DIC images. The filter scales a standard Gaussian filter (h_G) with the mean ($\langle h_G \rangle$) and a sensitivity factor ϕ as follows:

$$h_{SoG} = \lambda \left[h_G - \langle h_G \rangle \right] - \phi \cdot \langle h_G \rangle, \quad (10)$$

a general formulation of Equation 5. The switch parameter $\lambda \in (-1, 1)$ and depending on whether the image contains bright objects against a dark background e.g. DIC and fluorescence, or dark objects against a bright background λ is +1 or -1 respectively (Fig. S1), while the sensitivity factor ϕ is used to enhance the degree of contrast between fore- and background. The filtered image is thresholded based on a modified estimate obtained using Otsu's method (31), resulting in object detection.

The detection method appears to identify the majority of birefringent yolk granules in a DIC image-time series of *C. elegans* embryos as identifiable by eye (Fig. 1(a)) due to the enhanced contrast achieved by filtering, allowing objects to be segmented by automated threshold detection (Fig. 1(b)). To quantify the extent to of correctly detected yolk granules, we have used six randomly selected frames in the time series in two representative regions of interest (ROIs), one anterior and one posterior to account for any spatial differences (Fig. 2(a)) and marked yolk granules manually to serve as the ground truth (GT) of detection (Fig. 2(b)). The output from DICOT analysis was then classified based on the Euclidean distance of the granule coordinates (xy positions) detected by the algorithm to the 'true coordinate' into the following classes:

True positives (TP): The distance of the centroid identified by the algorithm lies within a threshold (τ_{dist}) distance of the interactively annotated point. A τ_{dist} of 2 pixels was chosen to account for human error while selecting centroid of granule.

False positives (FP): Detections obtained from the algorithm at a distance to the ground truth greater than τ_{dist} , are classified as false positives.

False Negatives (FN): All manual annotations that were not detected by the algorithm are classified as false negatives.

To quantify how well DICOT works at object detection, we estimate three variables: sensitivity (S), precision (P) and the F1-score. Sensitivity (S) is defined the ratio of correct detections by the algorithm (TP) by the sum of detected objects that were true yolk granules and those that the algorithm failed to identify but were true granules (determined by the GT), as described by the expression:

$$S = \frac{TP}{TP + FN} \quad (11)$$

An alternative measure, precision (P) is the fraction of correctly classified detections out of total detections from the algorithm as given by:

$$P = \frac{TP}{TP + FP} \quad (12)$$

Here the denominator sums over those objects the algorithm detected that were correct, as well as those it incorrectly detected (FP). Finally the F1-score combines both measures of P and S as:

$$F1 = \frac{2 \times P \times S}{P + S} \quad (13)$$

We find the precision, accuracy and F1-scores are optimized when the kernel size is close to the size of the objects being tracked, ~6 pixels for yolk granules and σ is in the range from 1 to 4, depending on the spread of the peak (Fig. 2(c-e)). Based on a comparison between manual detection (Fig. S3(a)) with SoG, Gaussian, inverted LoG and DoG based image filters (Fig. S3(b-d)), qualitatively SoG is comparable to LoG and DoG filtering (Fig. S3(e)). While results from SoG filtering are comparable within error-bars of the F-score, sensitivity and precision as compared to the other modified Gaussian filters, the outcome from SoG-based analysis is most robust to the method of object detection, whether centroid or regional intensity maximum (Fig. S4(a-c)). Our method allows by the user to make these tradeoffs, depending on the quality of the image data. For the *C. elegans* time-series we proceeded to track the mobility of granules using SoG filtering combined with automated thresholding and distance-based tracking, to quantify of spindle movement dynamics.

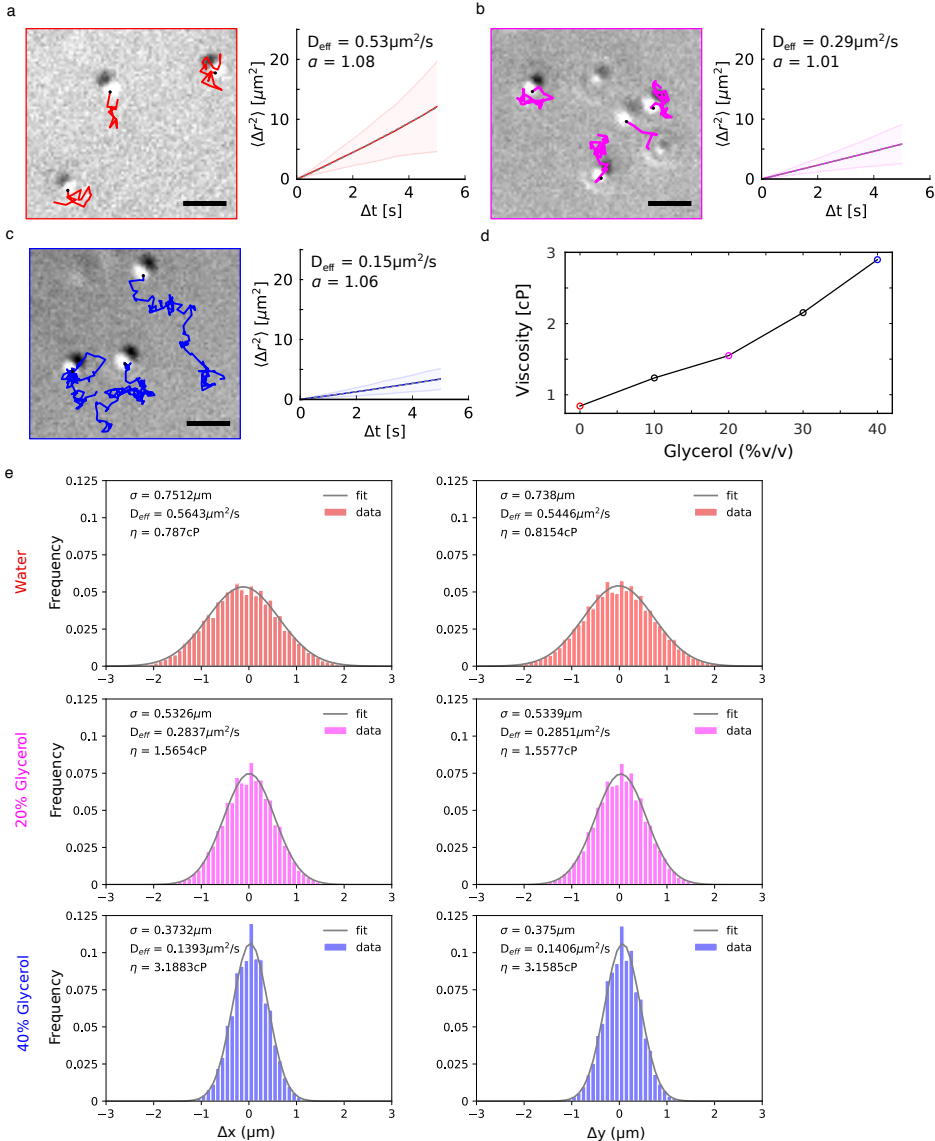


Figure 4: Microrheology of glycerol solutions from bead mobility. (a-c) Glycerol solutions of increasing concentrations with 1 μm diameter beads suspended in them were imaged to measure the bead mobility. The beads were tracked (colored lines) and the mean squared displacement \pm s.d. (line with grey area indicating s.d.) was calculated. Track colors correspond to (left to right) 0% (red), 20% (magenta) and 40% (blue). Scalebar: 2 μm . (d) The viscosities estimated these diffusing 1 μm beads in varying glycerol concentrations in water. (e) Histograms of the instantaneous displacement of beads in X and Y obtained from tracking were fit to a standard Gaussian. The samples were resuspended in (a) water and aqueous glycerol solutions of (b) 20% (c) 40% (v/v). The effective diffusion coefficient D_{eff} was then estimated based on $\sigma = \sqrt{2D_t}$ from the Gaussian fit and the Stokes-Einstein relation used to estimate viscosity η .

Oscillatory dynamics of yolk granules at Anaphase

Single celled embryos of *C. elegans* in anaphase experience cytoplasmic streaming in the mid-plane driven by MT-motor interactions observed in terms of yolk granule movement (32). Previous work that has examined the mobility of the spindle in the one-celled *C. elegans* embryo during anaphase has quantified the oscillatory nature of the spindle movement (20, 21, 27). Since yolk granules are thought to be passively mobile in the cytoplasm (17), our approach to particle tracking could provide a spatial map of this cytoplasmic mobility driven by spindle oscillations. We can successfully track multiple DIC image time series of the mid-plane of these embryos and classify them into anterior (A), posterior (P) or two transverse regions T1 and

T2 (Fig. 3(a)), since granules remain relatively restricted to a region of the embryo. The time-dependent displacement of granules along either the y-axis for regions A and P, or along the x-axis for T1 and T2, display oscillatory behavior that is captured by an average curve (Fig. 3(b)), obtained by iterative optimization to individual trajectories (Fig. S5). The oscillations along the two axes A-P and T1-T2 are out-of-phase as expected from spindle geometry and the incompressible nature of the cytoplasm. The dominant frequency of oscillation along both axes is 40 mHz based on Fourier analysis of average trajectories (Fig. 3(c)). Our estimate from the large statistics of granule movement is consistent with the reported frequency of 40 mHz of spindle pole oscillations measured by following a pair of centrosomes (20, 21, 27). The detailed spatiotemporal resolution obtained from our approach to cytoplasmic granule tracking, can in future help better understand the mechanics of incompressible flows and the mechanics of the MT-motor interactions, that drive the spindle oscillations.

Microrheology of beads in glycerol solutions

We test the quantitative accuracy of our approach to object tracking by quantifying the diffusive mobility of 1 μm polystyrene beads in multiple dilutions of glycerol solutions (0 to 40% v/v) from DIC image time-series. From the trajectories of the bead mobility, we estimated the mean squared displacement ($\langle r^2 \rangle$) as a function of time t of multiple beads and fit it to a model of diffusive mobility $\langle r^2 \rangle = 4D \cdot t^\alpha$ (Fig. 4(a-c)) as described in our previous work (29). The value of the anomaly exponent α obtained from fitting is ≈ 1 , confirming that bead mobility is diffusive. The diffusion coefficient D is then used to estimate the viscosity η (Fig. 4(d)) based on the Stokes-Einstein relation $\eta = k_B T / D 6\pi r$, where r is the granule radius and $k_B T$ the thermal energy scale. We also estimated the value of viscosity from the same trajectories by alternatively following a method originally described by Perrin (30) by fitting gaussian functions to the 1D displacement along x- and y-axes (Fig. 4(e)). Both methods yield viscosity values that are consistent with reported standard values (33). Thus, we believe our method can serve as a convenient tool for microrheology and mobility of label-free DIC imaging of micron sized objects, both intracellular and *in vitro*.

CONCLUSION

The yolk granule mobility in *C. elegans* embryos demonstrated here suggests the frequency of oscillation of granules matches that of the spindle movement. While on the one hand it confirms the passive nature of yolk granule mobility, it also provides a spatiotemporal readout of the forces that drive spindle motility. The previous estimates of the viscous drag acting on the spindles (17, 34) and more recent measurements of the viscoelastic nature of the cytoplasm (35), suggest the relevance of such a tool for the quantification of cytoplasmic streaming and the interactions of intracellular yolk-granules with MT-motor dynamics, could improve our understanding of the mechanobiology of asymmetric cell division, not just in the one-celled *C. elegans* embryo. In conclusion, our approach represents a robust filtering based approach to quantitative microrheology from both *in vitro* and *in vivo* DIC image time-series of micron sized objects.

ACKNOWLEDGMENTS

This work is supported by a BigData grant BT/PR16591/BID/7/673/2016 from the Dept. of Biotechnology, Govt. of India to CAA. YKJ was supported by a fellowship from Dept. of Biotechnology, Govt. of India. ARC was supported by the University Grants Commission (UGC F.2-14/2011 (SA-1)- Govt. of India, a postdoctoral fellowship from IISER Pune and CEFIPRA Grant 62T5-D. DK is supported by a fellowship from the Dept. of Biotechnology (DBT/JRF/BET-18/I/2018/AL/188) and CNRS-IISER Pune joint PhD program. We are grateful to Marie Delattre for valuable discussions about the nematode embryo data.

REFERENCES

1. Allen, R. D., G. B. David, and G. Nomarski, 1969. The zeiss-Nomarski differential interference equipment for transmitted-light microscopy. *Z Wiss Mikrosk* 69:193–221.
2. Zernike, F., 1942. Phase contrast, a new method for the microscopic observation of transparent objects. *Physica* 9:686–698.
3. Dixit, R., and R. Cyr, 2003. Cell damage and reactive oxygen species production induced by fluorescence microscopy: effect on mitosis and guidelines for non-invasive fluorescence microscopy. *Plant J* 36:280–90.
4. Guberman, J. M., A. Fay, J. Dworkin, N. S. Wingreen, and Z. Gitai, 2008. PSICIC: noise and asymmetry in bacterial division revealed by computational image analysis at sub-pixel resolution. *PLoS Comput Biol* 4:e1000233.
5. Rogers, S. S., T. A. Waigh, X. Zhao, and J. R. Lu, 2007. Precise particle tracking against a complicated background: polynomial fitting with Gaussian weight. *Phys Biol* 4:220–7.
6. Sliusarenko, O., J. Heinritz, T. Emonet, and C. Jacobs-Wagner, 2011. High-throughput, subpixel precision analysis of bacterial morphogenesis and intracellular spatio-temporal dynamics. *Mol Microbiol* 80:612–27.
7. Zeisel, A., A. Yitzhaky, C. Koerner, M. Lauriola, H. Cohen-Dvashi, W. J. Köstler, Y. Yarden, S. Wiemann, and E. Domany, 2013. qCMA: a desktop application for quantitative collective cell migration analysis. *J Biomol Screen* 18:356–60.
8. Piccinini, F., A. Kiss, and P. Horvath, 2016. CellTracker (not only) for dummies. *Bioinformatics* 32:955–957.
9. Athale, C. A., and H. Chaudhari, 2011. Population length variability and nucleoid numbers in Escherichia coli. *Bioinformatics* 27:2944–8.
10. Chalfoun, J., M. Majurski, A. Peskin, C. Breen, P. Bajcsy, and M. Brady, 2015. Empirical gradient threshold technique for automated segmentation across image modalities and cell lines. *J Microsc* 260:86–99.
11. King, S. V., A. Libertun, R. Piestun, C. J. Cogswell, and C. Preza, 2008. Quantitative phase microscopy through differential interference imaging. *J Biomed Opt* 13:024020.
12. Obara, B., M. A. J. Roberts, J. P. Armitage, and V. Grau, 2013. Bacterial cell identification in differential interference contrast microscopy images. *BMC Bioinformatics* 14:134.
13. Danuser, G., P. T. Tran, and E. D. Salmon, 2000. Tracking differential interference contrast diffraction line images with nanometre sensitivity. *J Microsc* 198:34–53.
14. Fanti, Z., M. E. Martinez-Perez, and F. F. De-Miguel, 2011. NeuronGrowth, a software for automatic quantification of neurite and filopodial dynamics from time-lapse sequences of digital images. *Dev Neurobiol* 71:870–81.
15. Bormuth, V., J. Howard, and E. Schäffer, 2007. LED illumination for video-enhanced DIC imaging of single microtubules. *J Microsc* 226:1–5.
16. Gönczy, P., H. Schnabel, T. Kaletta, A. D. Amores, T. Hyman, and R. Schnabel, 1999. Dissection of cell division processes in the one cell stage *Caenorhabditis elegans* embryo by mutational analysis. *J Cell Biol* 144:927–46.
17. Grill, S. W., P. Gönczy, E. H. Stelzer, and A. A. Hyman, 2001. Polarity controls forces governing asymmetric spindle positioning in the *Caenorhabditis elegans* embryo. *Nature* 409:630–3.
18. Blanchoud, S., Y. Budirahardja, F. Naef, and P. Gönczy, 2010. ASSET: a robust algorithm for the automated segmentation and standardization of early *Caenorhabditis elegans* embryos. *Dev Dyn* 239:3285–96.
19. Giurumescu, C. A., and A. D. Chisholm, 2011. Cell identification and cell lineage analysis. *Methods Cell Biol* 106:325–41.
20. Farhadifar, R., and D. Needleman, 2014. Automated segmentation of the first mitotic spindle in differential interference contrast microscopy images of *C. elegans* embryos. *Methods Mol. Biol.* 1136:41–45.
21. Cluet, D., P. N. Stébé, S. Riche, M. Spichty, and M. Delattre, 2014. Automated high-throughput quantification of mitotic spindle positioning from DIC movies of *caenorhabditis* embryos. *PLoS ONE* 9.

22. Gönczy, P., S. Grill, E. H. Stelzer, M. Kirkham, and A. A. Hyman, 2001. Spindle positioning during the asymmetric first cell division of *Caenorhabditis elegans* embryos. *Novartis Found Symp* 237:164–75; discussion 176–81.
23. Grill, S. W., J. Howard, E. Schäffer, E. H. K. Stelzer, and A. A. Hyman, 2003. The distribution of active force generators controls mitotic spindle position. *Science* 301:518–21.
24. Grill, S. W., K. Kruse, and F. Jülicher, 2005. Theory of mitotic spindle oscillations. *Physical Review Letters* 94:1–4.
25. Pecreaux, J., J. C. Röper, K. Kruse, F. Jülicher, A. A. Hyman, S. W. Grill, and J. Howard, 2006. Spindle Oscillations during Asymmetric Cell Division Require a Threshold Number of Active Cortical Force Generators. *Current Biology* 16:2111–2122.
26. Kozlowski, C., M. Srivastava, and F. Nedelec, 2007. Cortical Microtubule Contacts Position the Spindle in *C. elegans* Embryos. *Cell* 129:499–510.
27. Valfort, A.-C., C. Launay, M. Sémond, and M. Delattre, 2018. Evolution of mitotic spindle behavior during the first asymmetric embryonic division of nematodes. *PLoS Biol* 16:e2005099.
28. Khetan, N., and C. A. Athale, 2016. A Motor-Gradient and Clustering Model of the Centripetal Motility of MTOCs in Meiosis I of Mouse Oocytes. *PLoS Comput Biol* 12:e1005102.
29. Athale, C. A., A. Dinarina, F. Nedelec, and E. Karsenti, 2014. Collective behavior of minus-ended motors in mitotic microtubule asters gliding toward DNA. *Phys Biol* 11:016008.
30. Perrin, J., 1909. Mouvement brownien et réalité moléculaire [Brownian movement and molecular reality]. *Annales de Chimie et de Physique* 8:5–114.
31. Otsu, N. N., 1979. A Threshold Selection Method from Gray-Level Histograms. *IEEE Transactions on Systems, Man and Cybernetics* 9:62–66.
32. Shinar, T., M. Mana, F. Piano, and M. J. Shelley, 2011. A model of cytoplasmically driven microtubule-based motion in the single-celled *Caenorhabditis elegans* embryo. *Proc Natl Acad Sci U S A* 108:10508–13.
33. Segur, J. B., and H. E. Oberstar, 1951. Viscosity of Glycerol and Its Aqueous Solutions. *Industrial & Engineering Chemistry* 43:2117–2120. <https://doi.org/10.1021/ie50501a040>.
34. Grill, S. W., 2002. The mechanics of asymmetric spindle positioning in the *Caenorhabditis elegans* embryo. Ph.D. thesis, Physik-Department, Technische Universität München.
35. Garzon-Coral, C., H. A. Fantana, and J. Howard, 2016. A force-generating machinery maintains the spindle at the cell center during mitosis. *Science* 352:1124–7.